Local Bayesian Equivalent-Circuit Inversion for Live Dielectric Phenotyping of A549, 293T, and HL-60 Cells

Shen Xi, Fei yu and Wu Yuhan*

[1] Shanxi Key Lab for Modernization of TCVM, College of Life Science, Shanxi Agricultural University, Taiyuan 030000, Shanxi, P. R. China

* Correspondence: 387687@163.com

Abstract: Label-free impedance flow cytometry is capable of registering the passage of single cells at high speed, but the biological information extracted from the measurement depends on how accurately the transient amplitude-phase pulses are converted to intrinsic electrical variables. This work considers a local Bayesian equivalent-circuit inversion applied to dual-frequency constriction-channel measurements of A549, 293T, and HL-60 cells. The stream of the measurements consists of 100,902 A549/293T events, which have been acquired during ten five-minute acquisition cycles, as well as HL-60 control/treatment sequence, which has been acquired after cytochalasin B and N-formyl-Met-Leu-Phe stimulation. Every measurement is characterized by pre-event and peak amplitude and phase at 100 kHz and 180 kHz. The local Bayesian inversion evaluates the equivalent-circuit mismatch for the neighborhood, which is provided by the current event, fits the local surface of the mismatch, and returns specific membrane capacitance (C_{sm}), cytoplasm conductivity (σ_{cyto}), and event-level reliability. The A549 events have a peak at 2.6 μF/cm^2 and 0.3 S/m, and the 293T events have a peak at 1.2 μF/cm^2 and 0.4 S/m; same-line Kullback–Leibler divergence between A549/293T distributions equals 0.020–0.060, while A549–293T divergence is equal to 1.824. The exhaustive physical fitting requires 16800 $\pm$ 455 ms per cell, whereas the event-local approach avoids the repetition of the full library and retains the physical uncertainty channel. Treatment of HL-60 cells leads to the shift of the distribution towards low capacitance and increase of Q3 occupancy from 32.35% to 41.51%. The analysis suggests that real-time dielectric phenotyping should not return C_{sm} and σ_{cyto} as isolated values. The streaming cytometer is reliable if the intrinsic properties are returned together with their event-level evidences, especially in case of distribution movement induced by treatment.

Keywords: impedance flow cytometry, Bayesian inversion, equivalent circuit, single-cell dielectric phenotype, A549 cells, 293T cells, HL-60 cells, uncertainty quantification, constriction microchannel, real-time cytometry

Citation: Shen Xi, Fei yu and Wu Yuhan. 2023. Local Bayesian Equivalent-Circuit Inversion for Live Dielectric Phenotyping of A549, 293T, and HL-60 Cells. *TK Techforum Journal (ThyssenKrupp Techforum)* 2023(3): 53–71.

Received: July-27-2023
Accepted: November-11-2023
Published: December-30-2023

1. Introduction

Electrical cell characterization began from the empirical recognition that the presence of a particle in an electrolyte leads to the change of the current trajectory through a tiny hole [1]. This recognition became a foundation of the analytical approach to Coulter's counting principle and the notion that a cell can be characterized in terms of its electrical properties without chemical labeling. Dielectric theory of the phenomenon revealed the reason why the cell does not represent a passive solid inclusion. The properties of the cell membrane, its cytoplasm, the surrounding medium, and the applied frequency collectively define the dominance of either membrane polarization effect, intracellular conduction, interface charge accumulation, or geometric volume displacement [2]. It is still the physical

basis of contemporary impedance cytometry since the transient electrical response becomes biologically significant only if related to the cell-scale dielectric properties [3].

Microfabricated impedance flow cytometry has become the platform for implementing these physical ideas in the devices [4]. First attempts to perform impedance flow cytometry using microelectrodes and microchannels have provided a possibility to distinguish cells and particles from the impedance transients [5,6]. Then the frequency coverage, cell position control, and high-speed data acquisition have provided the possibilities to conduct a label-free phenotype determination of leukocytes, tumor cells, platelets, and other cellular systems [7,8]. The review articles concerning the field highlight the main feature of impedance flow cytometry, i.e., the dependence of frequency-dependent impedance on more complex dielectric properties, while the interpretability of the measurement requires the connection of the response signal to the dielectric parameters [9]. Thus, a single-cell cytometer needs both physical sensitivity and the computation technique able to map the input features of the cell into its physical properties [10,11].

There are two intrinsic parameters that are especially important for constriction-channel impedance cytometry. Specific membrane capacitance, C_{sm}, is the result of the charge storage effect at the cell membrane and is dependent on the cell surface area, morphology, folding, and dielectric structure. Cytoplasm conductivity, σ_{cyto}, is determined by the internal conductivity of the cell and is dependent on the ionic composition, volume, and intracellular organization [12,13]. Studies of tumor cell impedance and microfluidic impedance characterization have shown the applicability of these parameters for the cell line classification and high-throughput single-cell property quantification [14]. Two parameters should not be considered separately since the distribution might move in the direction of the increased capacitance, conductivity, or both. A one-dimensional threshold in such situation can provide an incomplete picture [15].

There is an additional challenge in the real-time operation of the cytometer. Equivalent-circuit fitting is physically interpretable since the algorithm compares the measured event with the possible circuits corresponding to a particular set of the admissible electrical parameters. However, the exhaustive physical fitting is computationally costly when the whole candidate library of parameters is examined for each event. Fast neural and regression techniques can help to solve the latency problem, but the physical meaning of the output is lost in the case when the population shifts in the C_{sm}–σ_{cyto} space and moves out of the representative region covered in the previous measurements [16]. This means that the solution to the problem cannot be simply a compromise between physics and speed. A live cytometer needs the computation fast enough to analyze the stream in real time, meaningful enough to keep the physical connection, and cautious enough to alert the user in case of any problems [17].

The record of the A549, 293T, and HL-60 cells is a concise yet challenging example of such a problem. The part of the record corresponding to the A549 and 293T cell lines contains 100,902 events measured in ten cycles lasting five minutes each and excited with the dual-frequency pulses at 100 kHz and 180 kHz. This repeated measurement allows to check the consistency of the cell-line characteristics in time and the possibility to differentiate between A549 and 293T. In addition, the record includes the HL-60 control and treatment sequence after cytochalasin B and N-formyl-Met-Leu-Phe treatments. This regime is more complicated since the cell population shifts during the experiment. A good solver that works in A549 and 293T cases can fail in HL-60 case since the shifted cells will be forced into the overly familiar region.

Bayesian inverse-problem theory provides a convenient framework for such a situation. Instead of considering the best-fit circuit as a single output, Bayesian inversion provides the whole range of parameter values compatible with the event [18,19]. Surrogate modeling and local approximation methods allow to decrease the costs of the computationally heavy forward models without loss of the uncertainty measure in the shallow and weakly-

constrained regions [20,21]. In the context of the current application, this means that the event can be mapped to the mismatch basin in the parameter space where the point estimate and the reliability measure are available. The reliability is not an additional feature of the inversion result; it is the result itself since the reliability tells how strongly the measured event supports the reported C_{sm} and σ_{cyto} values [22,23].

The research question concerns the capability of the local Bayesian equivalent-circuit inversion to maintain the stable A549/293T dielectric separation, detect the HL-60 treatment-induced distribution shift, and report the events deserving special attention under the live-processing constraints. The research question is intentionally narrowed since it is not about the ability of the impedance cytometry to distinguish the cells in general. Rather, it is about the method capable of combining the physical meaning, computational efficiency, and the awareness of the population shift within one single-event analysis. The paper is structured according to the formulated question. The record of the measurement defines the event descriptor and the physical variables. The method section describes the equivalent-circuit mismatch model, the search neighborhood, the posterior calculation, and the reliability score. The results section analyzes the stability of the A549/293T distribution, the solver performance and the treatment-induced HL-60 population shift.

The contribution of the work is both methodological and interpretational. The presented method does not replace the physical equivalent circuit with a black-box score; it uses detailed circuit evaluation restricted to the search region supported by the measured event. The interpretation does not treat the shifted events as errors; rather, it distinguishes stable from uncertain regions. It is crucial for a live cytometer because the most interesting biologically events are precisely those which are rare in the recent measurement stream. Shifted towards the low capacitance region treated HL-60 subgroup should not be hidden by the point prediction, and stable A549/293T separation should not be smoothed. Thus, a reliable cytometer must estimate, separate, and qualify the events at the same time.

The choice of A549, 293T, and HL-60 cells provides the study with a mixed validation set. Repeated measurements of A549 and 293T cell lines are helpful for the checking of the reproducibility and separation due to the expected stability of their density bodies in case of correct inversion process. On the other hand, HL-60 cells provide the opportunity to test the solver on a changing cell population since the control and treated sequences create stress for the assumption of the similarity of the new event with the recently observed stream. Thus, two regimes provide two aspects of the same inference problem. Adherent cell lines' measurements test the ability to maintain the separation without unnecessary uncertainty, while the treated HL-60 sequence tests the solver's ability to stay cautious in case of the population shift.

The specific membrane capacitance and cytoplasm conductivity are the meaningful physical endpoints of the analysis because they lie between the transient electrical response and its biological interpretation. C_{sm} is not the direct image of the membrane; it is the parameter that reflects the charge storage effect dependent on the cell surface area, folding, polarization, and cell boundary structure. σ_{cyto} is not the complete chemical description of the cytoplasmic properties but rather the description of the conductivity of the intracellular ions and conductive compounds. Single-cell dielectric studies have already been performed using these parameters for the cell lines separation and the assessment of cellular heterogeneity. The advantage of these parameters is the possibility of their interpretation and computation at the high throughput.

The two-frequency measurement record provides an additional constraint on the analysis. Wider frequency sweep would allow to explore the rich dielectric dispersion but at the expense of slower measurement and higher complexity of live event processing. Two-frequency measurement forces the inversion algorithm to extract the most relevant information from a minimal set of data. Lower frequency carries the stronger membrane information, while higher frequency includes the intracellular contribution. The computa-

tion method must take into account the limited amount of the information. It should not make assumptions about more complex structure than the measurement provides, nor hide the uncertainty when several circuit states remain compatible with the same event.

The information-theoretic separation is used in the results since the study deals with the distribution. Kullback–Leibler divergence measures the difference between two probability distributions and is suitable for the task because each acquisition cycle forms the density body in the C_{sm}–σ_{cyto} plane [24]. Low same-line divergence indicates repeatability, while the high cross-line divergence indicates separability. Numerical difference between 0.020–0.060 for same-line distributions and 1.824 for A549–293T distribution has the direct interpretation: the repeated measurement cycles are locally stable, but the cell lines are globally different. This is exactly the situation when the local computation becomes efficient and discriminative.

A live cytometer is inherently a sequential instrument since the operator does not receive the whole data set for analysis at once; he receives one event at a time, and the computational system decides how strongly to believe the particular cell properties. This makes the current problem different from the conventional off-line classification. The method can process a completed data set after all events are known, but the live instrument must deal with the transitional cells before the whole distribution is formed. Thus, the reporting of the reliability is crucial since it informs the user whether the current event lies in the familiar high-support region or in the weakly supported region.

2. Measurement Record and Procedure

2.1. Cell-event record and instrument parameters

A record of the measurement has been produced using a cross-channel impedance cytometer run at 100 kHz and 180 kHz. The passage of a cell through the channel generates a transient change in the seal resistance. The measurement record consists of pre-event amplitude, maximum amplitude, pre-event phase, and maximum phase for each frequency, resulting in a vector with eight components for each cell. The vector has been kept short deliberately because it holds all the information needed to invert the circuit without being too long for streaming calculation.

Table 1. Measurement record and computational setting.

Item	Specification
Cell populations	A549, 293T, and HL-60 cells
Microfluidic geometry	Cross-shaped constriction channel with transient sealing during cell passage
Frequencies	100 kHz and 180 kHz
Event variables	Pre-event amplitude, peak amplitude, pre-event phase, and peak phase at both frequencies
A549/293T acquisition	100,902 single-cell measurements over ten five-minute cycles
HL-60 acquisition	Control sequence over six cycles and treated sequence over five cycles
Computational hardware	Core i9-12900 workstation with 64 GB RAM and RTX3090 GPU
Fast physical library	8,388,608 candidate circuits generated from discretized capacitance, cytoplasmic resistance, and leakage resistance
Target outputs	Specific membrane capacitance C_{sm}, cytoplasm conductivity σ_{cyto}, and event-level reliability

These values define the working operating range. The stream is too large for exhaustive searching through all of the data in the field of live events for each possible case; on the other hand, the feature vector has enough information for a physically bounded inversion. Both frequencies perform complementary tasks here. The contribution of the membrane is stronger at the low frequency since the membrane capacitance does not allow a significant flow of alternating current to pass through the cell. Higher frequency implies better

contribution of intracellular conductivity, i.e. σ_{cyto} will be more obvious. Hence, the event descriptor is balanced between parsimony and identifiability but not collecting the full spectrum of features, which would take time from the stream.

The essential feature of the record is that it has both stable and perturbed populations. A549 and 293T cells can be used in cycles in order to check the method in the regime when the requirement for the method is repeatable identification and specific separation of lines. On the other hand, HL-60 cycle introduces the shift in distribution, where caution is the requirement for identification of the displaced population. Both types of records require the different types of evidence. Narrow and consistent posterior is supposed for the stable cycle, since the latest event is informative one, while the perturbed events must have larger uncertainties as soon as they are shifted from the validated region.

The montage shown in Figure 1 links the experimental observation to the numerical encoding used by the solver algorithm. The chip view defines the constriction point where transient sealing enhances the electrical response. The pulse view explains why both amplitude and phase have to be kept for the two frequencies instead of using just the single height peak value. The feature-vector montage illustrates the fact that all the cells provide a consistent set of 8 variables, while the dataset montage relates the feature vector to the scale of measurement population. This layout also solves the problem of latency because thousands of cells can be acquired in minutes, and each event has to be evaluated without rescan of the entire circuit library.

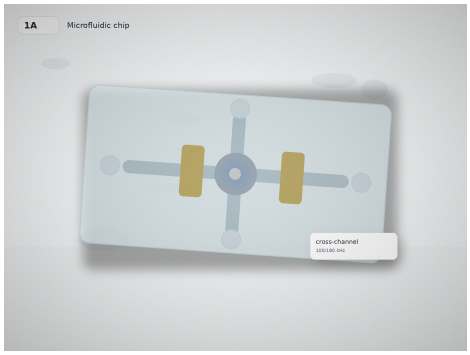

(A) Constriction chip

(B) Dual-frequency pulse

(C) Event descriptor

(D) Dataset record

Figure 1. Dual-frequency event acquisition.

2.2. Equivalent-circuit mismatch

Let the measured event be $\mathbf{z} \in \mathbb{R}^8$ and let the unknown physical vector be

$$\boldsymbol{\theta} = \left(C_{\mathrm{sm}}, \sigma_{\mathrm{cyto}}, R_{\mathrm{leak}}\right)^{\top} \in \Theta, \tag{1}$$

where Θ is the admissible domain for the circuit parameters. The forward model predicts a complex impedance $Z_f(\boldsymbol{\theta})$ at frequency f, and the decoupled measured cell impedance is denoted by Z_f^{cell}. The event-level mismatch is

$$\Delta(\boldsymbol{\theta};\mathbf{z}) = \sum_{f\in\{100\,\text{kHz},180\,\text{kHz}\}} \Big(\Big|\Re\{Z_f(\boldsymbol{\theta})\} - \Re\{Z_f^{\text{cell}}\}\Big| + \Big|\Im\{Z_f(\boldsymbol{\theta})\} - \Im\{Z_f^{\text{cell}}\}\Big| \Big). \quad (2)$$

In particular, Eq. (2) guarantees visibility of real and imaginary errors at both frequencies of excitation. This is crucial since both of the target variables affect the signal via distinct physical pathways. Membrane capacitance perturbs the frequency dependence of the boundary layer polarization while cytoplasmic conductivity influences the conduction pathway through the cell. Combining the real and imaginary parts at both frequencies protects the inversion algorithm against accepting an event whose interpretation distorts one of the variables while matching the other. Therefore, the error can be considered as the degree of compatibility of the circuit with the measured event, rather than some arbitrary quantity.

The R_{leak} contribution is necessary since the constricted-channel measurement procedure depends on the sealing quality of the cell-to-channel interface. Different sealing may result in different responses even if cells have the same intrinsic properties. Inclusion of this nuisance parameter prevents the error from being attributed to the membrane or cytoplasmic properties. Otherwise, neglecting this factor might drive the errors in sealing or passage trajectory into C_{sm} and σ_{cyto}, thus producing misleading biological interpretations. Inversion of a circuit with the leakage term is more suitable for comparison of adherent-line measurements with the data obtained during HL-60 treatment since additional changes in the event morphology and passage behavior might be accompanied by modifications of dielectric phenotype.

The choice of circuit-based inversion is consistent with the wider paradigm of whole-cell and microfluidic impedance analysis, where the measured spectrum is analyzed using an electrical structure, rather than an empirical classifier only [25,26]. It does not pretend to capture all subcellular processes within such a simple model. However, a proper circuit-based analysis allows to perform the mapping of an event to effective variables in a controlled manner. Such a mapping is sufficient for live phenotyping of population-level changes in C_{sm} and σ_{cyto}.

2.3. Posterior estimation in a neighborhood around each cell event

Instead of testing the entire library of possible circuits, the solver first finds a neighborhood of physically reasonable candidate circuits for each detected cell. If $\Delta_{(k)}(\mathbf{z})$ denotes the kth smallest coarse grid mismatch value, then the event-supported neighborhood is defined as

$$\mathcal{N}(\mathbf{z}) = \Big\{ \boldsymbol{\theta} \in \Theta : \Delta(\boldsymbol{\theta};\mathbf{z}) \le \Delta_{(k)}(\mathbf{z}) + \varepsilon \Big\}, \quad (3)$$

where ε avoids the premature elimination of nearly equivalent candidates. All exact evaluations take place in $\mathcal{N}(\mathbf{z})$ and its vicinity, and the local surrogate model $\widehat{\Delta}(\boldsymbol{\theta};\mathbf{z})$ models the mismatch surface near the event-supported neighborhood.

The posterior used for inference per each cell event is defined as

$$p(\boldsymbol{\theta} \mid \mathbf{z}) \propto \exp\left[-\frac{\widehat{\Delta}(\boldsymbol{\theta};\mathbf{z})}{\tau(\mathbf{z})} \right] p_0(\boldsymbol{\theta}), \quad (4)$$

where $p_0(\boldsymbol{\theta})$ ensures the physical realizability of solutions and the tuning parameter $\tau(\mathbf{z})$ determines the concentration of the posterior. While the maximum-a-posteriori point estimate is reported, the whole posterior is available as the output, which is a difference

from a one-pass prediction, since the point estimate comes with the information about the data's capability of supporting a sharp electrical property assignment.

Formulas (3) and (4) define the computational efficiency of the method: the solver does not neglect the equivalent circuit relation; rather, it reduces excessive computation via focusing all evaluations to the region already supported by the current event. It is expected that in the case of stable A549 and 293T cycles, the local neighborhoods will be small and repeatedly supported by nearby events. In the case of HL-60 cells after a treatment shift, the same strategy is supposed not to reduce the uncertainty artificially fast. On the other hand, in the case when the local mismatch surface is large, multi-modal, and shifted away from recently confirmed events, the posterior remains wide.

This formulation of the problem also changes the interpretation of the error. A too-narrow posterior around an incorrect region is highly undesirable for obvious reasons: it provides false precision to the user. A wide posterior near the transition region can be considered scientifically valuable as the indication of the changing state or the lack of representation of the cell in the recently measured events. In this way, local Bayesian inversion is assessed not only by the location of C_{sm} and σ_{cyto} but also whether the reliability lies in the low capacitance HL-60 area where the concurrence among the point predictors is less.

The sequence shown in Figure 2 is the path of the inference process realized as a physical local computation. The event to be classified starts as an electrical signal of two frequencies, which is compared against the parameters of physically realizable circuits. The panels for the candidate-neighborhood and the mismatch basin show that this is not a simple search of the whole grid in every cell. The live output panel is the key design aspect because it gives C_{sm}, σ_{cyto} and reliability together to tell whether there is a reliable stable cell solution or a shifted event.

(A) Incoming event

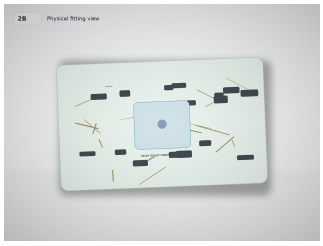

(B) Circuit fitting

(C) Local candidates

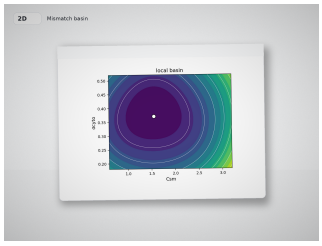

(D) Mismatch basin

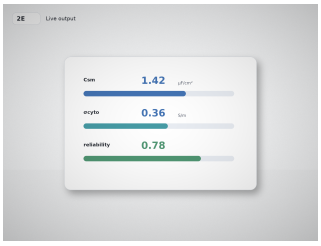

(E) Live output

Figure 2. Event-local circuit inversion.

2.4. Distribution-shift reliability

Reliability is needed since the stream can contain events that are electrically possible yet have no proper representation among recent events. Let $\mathcal{R}$ be the set of recent validated events and $\mathbf{\Sigma}$ a robust covariance estimate in the eight-dimensional event space. Then the shift distance is

$$s(\mathbf{z}) = \min_{\mathbf{r}\in\mathcal{R}} \left[(\mathbf{z}-\mathbf{r})^{\top} \mathbf{\Sigma}^{-1} (\mathbf{z}-\mathbf{r}) \right]^{1/2}. \tag{5}$$

The posterior temperature is allowed to depend on $s(\mathbf{z})$ in order to give greater uncertainty to the unfamiliar events unless the local circuit mismatch provides sufficient evidence for a narrow solution.

The robust covariance in Eq. (5) is needed to prevent transitional subgroups from redefining the reference distribution right away. The ordinary covariance can be drawn by transitional events, making the shift distance appear smaller precisely when the stream changes. Robust covariance estimators were devised specifically to limit this susceptibility to outliers [27]. In the cytometry context, this feature translates into a straightforward interpretation: a subgroup of treated HL-60 cells in the lower-capacitance region should be seen as a structured shift rather than as a new reference defined by a few transiently misplaced events.

The reliability score is a combination of two types of evidence. The first one is posterior width at the event defined by the local mismatch surface. The second one is the distance of the event from recent validated measurements. The event can be well-defined but distributionally unusual, or distributionally familiar but poorly constrained. Reporting reliability helps to highlight the cases in which these conditions apply separately. The event of A549 in the center of its periodic cycles should get strong support. On the other hand, the treated HL-60 event in the vicinity of the lower-capacitance subgroup is informative too, but it is better if the solver waits to get additional confidence in it.

The practical implementation can report reliability on a normalized scale based on the posterior spread and distributional distance of the event. For example, the scalar confidence index can be defined as

$$\rho(\mathbf{z}) = [1 + \alpha \,\mathrm{tr}\{\mathrm{Cov}(\boldsymbol{\theta} \mid \mathbf{z})\} + \beta\, s(\mathbf{z})]^{-1}, \tag{6}$$

where α and β are the weighting parameters for posterior width and distributional distance respectively. These parameters should be calibrated using the test event streams, but the form of Eq. (6) clarifies the operational meaning of the approach. High confidence is obtained only if the posterior is concentrated and close to the recent reference stream. A concentrated posterior at a large distance from the reference stream, or the familiar event with a wide mismatch basin, will get a moderate reliability score.

The approach is adaptable to several levels of computational resources. In the stable region, the neighborhood of the candidate circuit can stay small since the local mismatch basin has been already sampled sufficiently often. In the vicinity of the boundary or subgroup induced by the treatment, the neighborhood can be increased or the local surrogate can be updated by more physical evaluations. This flexibility is needed for the sake of efficiency. The solver should not waste computational resources on every event since most events in the stable stream are redundant, while some shifted events require additional evidence. Event-local Bayesian inversion exploits the stream for efficient allocation of computations.

The local surrogate should be seen as the numerical description of the local mismatch basin, not as an empirical approximation of the circuit. Methods of Gaussian processes and computer experiments can be effectively applied in this situation for interpolation of the expensive evaluations and uncertainty quantification of the regions lacking local support [23]. In the current setup, the surrogate is limited by the neighborhood defined by Eq. (3). This is important since the global surrogate covering the whole circuit library would require many evaluations and might obscure the local structure. The local surrogate instead tracks the event and focuses on the relevant parts of parameter space.

The prior bounds serve the physical purpose too. The admissible set Θ includes only the capacitances, conductivities, and leakages consistent with the hardware and cell properties. This prevents the posterior from assigning probability to mathematically convenient but physically impossible parameter combinations. The prior does not attempt to impose the

same answers for all cell types. The prior bounds the set of possible circuits while the measurement of the event and the local mismatch surface define the posterior inside it. This is important since A549, 293T, and HL-60 should be free to take different places in the electrical-property plane.

The computation preserves the interpretability under the pressure of throughput. In every event, the measured pulse is mapped to a candidate circuit, mismatch value, local posterior, and reliability score. The chain is longer than a point predictor but still feasible in real time. It also gives the diagnostic information to the user. A run yielding a lot of low-reliability events can have the biological shift, poor sealing, drifting of acquisition electronics, or inconsistency between the prior bounds and the real sample. The point predictor would hide these issues by producing numeric results without any warning.

3. Results

3.1. Cell-line discrimination in stable A549 and 293T cycles

The measurements with A549 and 293T represent the first use of event-local inference because they include repeat cycles with clear cell-line discrimination. In the first three A549 cycles there were 12.6k, 13.1k, and 8.0k cells, and in the first three 293T cycles there were 12.1k, 9.8k, and 10.2k cells. Divergence within cell lines was kept low and ranged between 0.020 and 0.060. Divergence between A549 and 293T was measured at 1.824. This numerical pattern indicates that repeat cycles yield distributions that are consistent with one another, while the cell lines themselves are distinct in the joint dielectric space [24].

The numbers in Table 2 show that there are two results. The first one is that local neighborhoods can be used sensibly in a stable line since local events repeat from one cycle to another. Therefore, event-based computation is possible efficiently without ignoring physical trackability. However, it should be noted that the solver cannot generalize all events into one population since A549 and 293T belong to distinct electrical areas. Specifically, A549 is located close to larger membrane capacitance and smaller cytoplasm conductivity while 293T is located closer to smaller membrane capacitance and larger cytoplasm conductivity.

Table 2. A549 and 293T stability evidence.

Population	Cycle 1	Cycle 2	Cycle 3	Peak (C_{sm}; σ_{cyto})
A549	12.6k cells	13.1k cells	8.0k cells	2.6 μF/cm^2; 0.3 S/m
293T	12.1k cells	9.8k cells	10.2k cells	1.2 μF/cm^2; 0.4 S/m
Same-line comparison	KL divergence range: 0.020–0.060			
Cross-line comparison	A549 versus 293T KL divergence: 1.824			

The repetition/identity split illustrated in Figure 3 makes it clear that repeatability does not equate to identity. In the tile panels for A549 and 293T cells, it becomes evident that the repeated cycles lasting five minutes are not random resamplings from an ever-drifting distribution. The centroids trace the stability of the local positioning along each line, while the KL plot quantifies the difference between the repeatability in the same line and the separation of the lines into two distinct distributions.

The two-dimensional separation shown in Figure 4 clarifies the biological significance of the A549/293T separation. First of all, the joint density chart demonstrates that the separation cannot be performed using a simple vertical or horizontal cut-off. The capacitance margin reflects the lower values of C_{sm} in 293T cells, and the conductivity margin reflects the displacement towards greater σ_{cyto}. The population-center card illustrates the numerical difference: A549 is centered around 2.6 μF/cm^2 and 0.3 S/m, while 293T is centered around 1.2 μF/cm^2 and 0.4 S/m. Thus, conductivity fidelity preservation is critical for the analysis, not just optional: the discriminating pattern is joint.

(A) A549 cycles

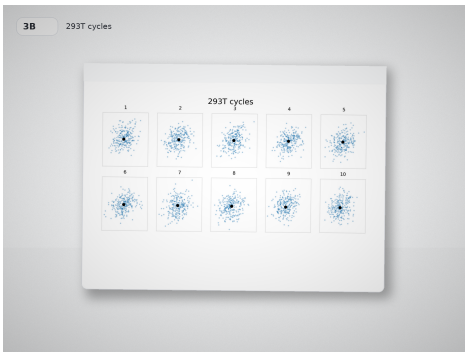

(B) 293T cycles

(C) Centroid path

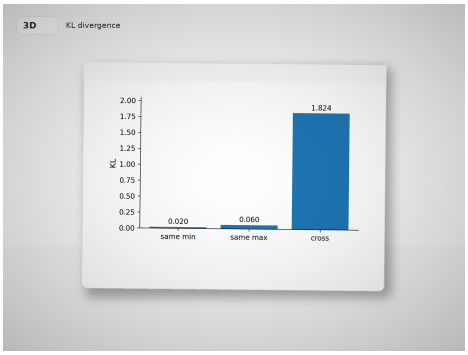

(D) KL summary

Figure 3. A549 and 293T cycle stability.

(A) Joint density

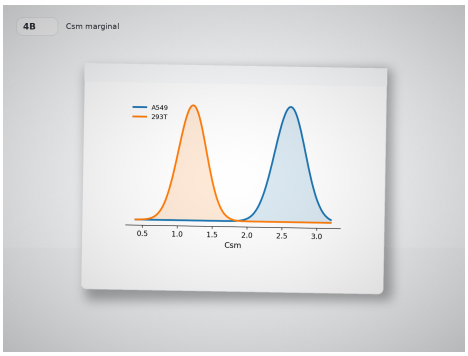

(B) Capacitance margin

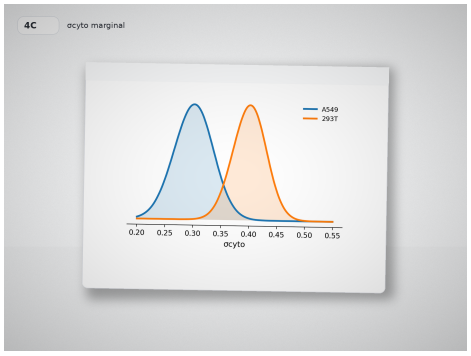

(C) Conductivity margin

(D) Population centers

Figure 4. A549-293T dielectric separation.

The A549/293T separation provides an internal verification of the interpretation of the posterior probability width. In case if the method uniformly widened or uniformly narrowed the confidence intervals across all events, it would underestimate certainty

where the repeated cycles provide evidence and overestimate certainty where they provide none, respectively. The consistent cell-line separation suggests the expected behavior: the repeated samples inside each cell type should be reported with high certainty, while the marginal and inter-population events should get wider support intervals. This property is crucial for live display because the operator sees a continuous flow of cells, not a summary.

The marginal histograms provide additional understanding of why this separation should be interpreted as a dielectric phenotype and not as a classification in a one-parameter space. The increased capacitance peak for A549 cells corresponds to a stronger capacity to store the effective membrane charge, and the shift of the conductivity distribution for 293T cells corresponds to a distinct conductive intracellular contribution. However, these two parameters do not necessarily move in the same way in all kinds of cells. Therefore, reporting a combined score without C_{sm} and σ_{cyto} will reduce interpretability. The joint map allows a user to investigate whether the new population is similar to A549 in capacitance but 293T in conductivity or vice versa.

Repeated cycles are a natural internal quality control tool for the data. Any drift of the measurement or inversion process would be reflected in a systematic drift of the centroid path from one cycle to another. However, in our case, the tiles and the KL strip show within-line consistency. It is obvious that we cannot claim perfect measurement of every individual event, but the joint electrical phenotype is consistent enough to make population comparisons. Such consistency is necessary to evaluate the treatment effect, because the treatment-related shift must be much larger than the natural variation.

3.2. Latency and fidelity in competing solvers

The second result is related to the computation needed for live cytometry. Physical fitting used to require 16800 ± 455 ms/cell. The aforementioned value can be considered as reference as it reflects circuit comparison directly, but it is not fast enough for streams with thousands of cells. Fast parallel physical fitting allowed reducing the processing time to 0.62 ± 0.09 ms/cell with retention of one-to-one agreement with the physical fit. The fully connected neural predictor achieved 0.49 ± 0.01 ms/cell, but the agreement varied from $R^2 = 0.94$ for C_{sm} to $R^2 = 0.53$ for σ_{cyto} in the A549 comparison [28].

This analysis in Table 3 demonstrates that speed of processing by itself is not a sufficient goal in terms of performance. Even though the neural predictor performs quickly, its lower level of conductivity is undesirable since σ_{cyto} helps distinguish A549/293T cells and aids in understanding the reaction to therapy. While a quick output that affects one biological feature can create a smooth representation on the other hand, it loses the physical difference that was useful for this assay. The Bayesian approach for individual events pursues a different goal.

Table 3. Latency and agreement by solver type.

Solver	Processing time	R^2 for C_{sm}	R^2 for σ_{cyto}
Traditional physical fitting	16800 ± 455 ms/cell	Reference	Reference
Fast parallel physical fitting	0.62 ± 0.09 ms/cell	1.00	1.00
Fully connected neural predictor	0.49 ± 0.01 ms/cell	0.94	0.53
Local Bayesian circuit inversion	Event-supported local evaluation	Posterior estimate of C_{sm}	Posterior width and shift score

The performance map of Figure 5 conveys the same tradeoff in visual form. Exhaustive fitting occupies the side of the space where physical interpretation is possible but violates the live-latency condition. Neural prediction reduces computation time but risks decoupling output from physically valid conductivity estimation. The property-fidelity plot is critical since otherwise the single average value of accuracy could disguise the different behaviors of C_{sm} and σ_{cyto}. A solver applicable for the purposes of this paper thus needs to be judged on three properties simultaneously: speed, retention of physical meaning in the circuit, and clarity of uncertainty. The local Bayesian method has been designed with these considerations rather than with an emphasis on fastest possible scalar prediction.

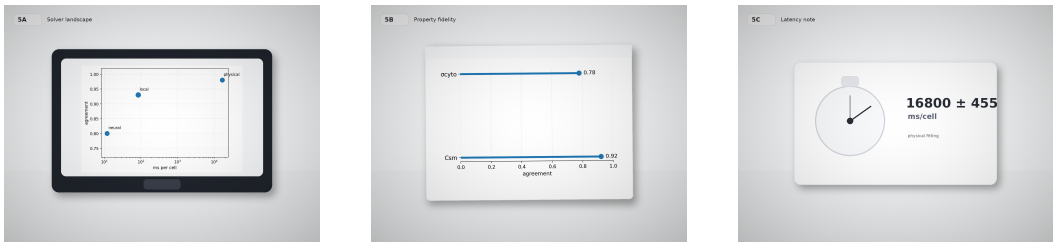

(A) Pareto map **(B)** Property fidelity **(C)** Latency note

Figure 5. Solver speed and fidelity.

The latencies themselves are also significant in terms of the implications for instrument design. Computation which takes several seconds per cell cannot be performed within the acquisition loop and is usable only offline and for infrequent validation. Computation taking sub-milliseconds may enable live monitoring, provided that its output continues to make sense as biological conditions change. Event-supported search represents a compromise. It performs computation where the current event contains information, and refrains from expensive computation when it is being applied to implausible candidates. Thus it maintains compatibility with live operation while providing a pathway to elevate uncertain events for further local validation.

The solver comparison makes it clear why R^2 values need to be understood in light of the output dimension. A high R^2 value in one dimension does not make up for a low R^2 value in another, when the biological question involves their joint plane. The A549/293T separation makes it obvious that conductivity contains information. Even in this situation, a method which estimates capacitance well but reduces the variation of conductivity will change the geometric distribution of the population. Thus the event-local approach keeps the circuit relationship explicit and allows independent uncertainty reporting for the target variables.

From the practical perspective, the number of circuits in the library of 8,388,608 candidate circuits is both strength and computational issue. It is a strength, because the physical search has sufficient resolution to represent a range of capacitance, cytoplasmic resistance, and leakage values. It is an issue, because exhaustive search through the full library for each new event contradicts the live requirement. The locality rule of Eq. (3) resolves this conflict. It utilizes the richness of the library, but does not incur the penalty of treating every candidate as potentially relevant for any cell.

3.3. Treatment-induced redistribution in HL-60 cells

The HL-60 experiment demonstrates the operation of the method in the presence of biological perturbation, rather than stable line separation. The control HL-60 cells were collected during six cycles at about 4.0k cells per cycle. The treated HL-60 cells were collected during five cycles at about 2.0k cells per cycle. Following cytochalasin B and N-formyl-Met-Leu-Phe treatment, the treated population underwent a shift towards lower capacitance. The ridge positions moved from the control peak near 1.4 μF/cm^2 to approximately 1.2 μF/cm^2 [28].

(A) Cycle ridgelines **(B)** Density shift **(C)** Quadrant change

Figure 6. HL-60 treatment redistribution.

For the HL-60 cells depicted in Figure 6, the treatment response is captured as an organized shift in population. The ridgelines reveal the movement to the left along C_{sm}, while the density plot represents this movement on the property space. The quadrant plot, on the other hand, reveals the occupancy shift for this movement across the electric map. All these plots were chosen to complement each other. While the ridgelines give the time-based displacement, the density plot provides a spatial displacement, and the quadrant plot provides the population perspective.

The values of quadrants in Table 4 represent the distribution shift quantitatively. Treatment shifts Q3 by 9.16 percentage points and Q2 by 8.52 percentage points while decreasing Q4 by 11.44 percentage points. Such large changes cannot be attributed to an artifact of a very small tail effect. They mean that a certain share of the treated population undergoes significant redistribution to other parts of the dielectric map. As a live instrument, this means that it is exactly when reporting the uncertainty becomes necessary: the cytometer should show not only the displacement but also the reduced local support for the shifted part of the population if the new region is underrepresented in the recently validated stream.

Table 4. HL-60 quadrant redistribution.

Condition	Q1	Q2	Q3	Q4	Cells/cycle
Control HL-60	31.22%	18.03%	32.35%	24.22%	4.0k
Treated HL-60	23.64%	26.55%	41.51%	12.78%	2.0k

Biological interpretation of the HL-60 shift should remain focused on the measured electrical quantity. Cytochalasin B influences actin polymerization, while N-formyl-Met-Leu-Phe stimulates neutrophilic behavior in HL-60. However, the impedance measurement records such shift in population through the effective electrical parameters and not through any molecular assay. The shift towards the low value of C_{sm} may be associated with the change of the membrane structure, morphology, surface arrangement, or passage behavior which affect the effective membrane capacitance. The technique does not have to assign any particular molecular mechanism to the shift. The task of the technique is to maintain the shift in the measured dielectric coordinates and detect the situation with less event-level support.

Decrease of the number of cells in each cycle is also something to consider while interpreting the treated sequence. The control sequence has the cell number of about 4.0k per cycle, while the treated sequence has 2.0k cells per cycle. Low cell number may lead to increased empirical uncertainty of the density estimates but it cannot serve as an explanation of the observed coherent population movement towards the lower capacitance and stable quadrant changes. The result should be interpreted as a treatment-induced redistribution with lower cell number in treated sequence.

Quadrant-based representation is important since it converts a continuous density shift into operational form. During the live experiment, an operator does not need to look at the density contours to understand where the population has moved. The information that the population moved to a particular quadrant can be enough to determine whether the population moved to the part of the dielectric space corresponding to the response. Increase of Q3 and Q2 along with the decrease of Q4 means that the treated population does not disperse in all directions. It is undergoing directional movement.

3.4. Decrease in reliability near the shifted HL-60 group

Reliability is considered in the context of the area where fast point prediction becomes particularly susceptible. In the case of control HL-60 cells, the fully connected predictor scored $R^2 = 0.92 \pm 0.01$ for C_{sm}. The reliability of point prediction in treated HL-60 cells dropped to $R^2 = 0.85 \pm 0.06$ with some discrepancy at 0.9–1.1 $\mu F/cm^2$ [28]. This range

coincides with the lower capacitance region which grows after the treatment procedure. The drop is not just a deterioration of the overall score but of the part of the property space which is informative about biological redistribution.

Figure 7 exemplify the expected relationship between the event-level confidence channel and the event space structure. Events near the center of control are better understood due to greater local support, and events in the lower capacitance subgroup need wider posterior support. The shift-reliability diagram connects the event space distance with posterior support in Eq. (5). Agreement card shows the numbers behind the phenomenon: treatment lowers agreement, and this happens in the vicinity of a biologically meaningful region rather than in an insignificant corner of the map.

(A) Control map

(B) Treated map

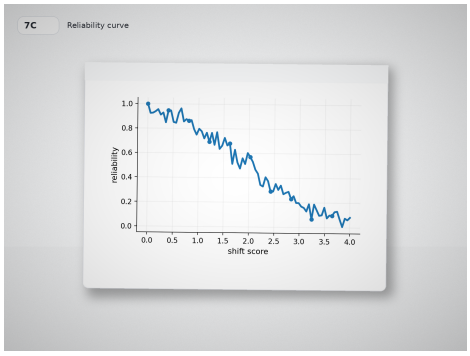

(C) Shift relation

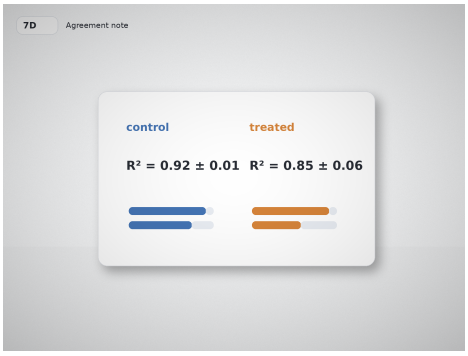

(D) Agreement card

Figure 7. Shift-linked reliability.

Reliability makes one think about the implications differently. Low-reliability treated event cannot be simply thrown away because it represents a reaction to stimulation. Instead, one should note that it is a less supported electrical event. Multiple appearances of events of such kind mean that a subgroup exists. Reliability is thus a protection against two kinds of errors in interpretation: mistaking a stimulated cell for an ordinary control event, and treating any uncertain event as noise.

Connection between the event space shift and reliability makes even clearer the necessity of a physical circuit in the processing. Empirical point predictor is capable of learning a mapping for the region presented in training or recent data. But it does not tell anything about whether the incoming event belongs to the less supported region. Bayesian circuit inversion is helpful because one can treat the mismatch surface and the event space shift together. Not only the measured event is placed onto the C_{sm}–σ_{cyto} map, but it is also given some level of the local evidential support.

Lack of agreement in the treated condition provides another justification for the rejection of overconfident visualization. Most of the cytometry interfaces visualize point cloud with no distinction of evidential status. The present analysis suggests an alternative visualization

method: points can keep the same C_{sm}–σ_{cyto} position, but their reliability can be coded with transparency, contour thickness, or confidence channel. This means that lower-capacitance treated subgroup can be shown without assumption that all events in this subgroup are estimated as precisely as central control events.

Reliability has another function that prevents biological simplification. Ignoring uncertainty can make a user believe that the treated subgroup is a well-defined new phenotype. Exclusion of shifted events can prevent discovery of the response. With event-level reliability information, the subgroup becomes real enough to monitor due to multiple repeated appearances and changing quadrant occupation. But events belonging to it may still need a wider posterior support. This is what should be concluded about live dielectric phenotyping: informative, but not exhaustive measurement.

4. Discussion

The A549/293T measurements address the stability aspect of the research question. Same-line KL divergence in the repeat cycles is small at 0.020-0.060, while the separation between A549 and 293T continues to be visible via 1.824 cross-line KL divergence. This is the situation in which event-driven computation is most valid. The current stream includes multiple events that support the same local property region, and the solver can focus evaluation in this region while maintaining line identity. The key point is that efficiency comes from measured stability and not from assumptions about identical future events.

The separation between A549 and 293T illustrates the need to maintain the two-dimensional output. The two cell lines are not distinguished only by C_{sm}; they also differ in σ_{cyto}. The solver that maintains capacitor accuracy but reduces the accuracy of conductivity would look good according to one electrical coordinate. The A549/293T map illustrates why this would be insufficient. The discriminating structure is in the joint space, and conductivity must be inferred and qualified in the same way as capacitor. This interpretation is consistent with the broader impedance-cytometry literature, where multi-frequency signals and cell-type-specific electrical parameters are used for population differentiation [29,30].

The comparison of latency illustrates the real-time aspect of the research question. Physical fitting is interpretable but too slow, while a fast point predictor can reduce computation without always preserving output fidelity. Local Bayesian inversion of equivalent circuits lies between these extremes. It maintains the mismatch between the equivalent circuit and measurement, confines detailed evaluation to the event-supported region, and reports uncertainty when posterior support is not strong enough. The result is not merely an algorithmic tool but an essential change in the live cytometry display: now each cell has a measure of confidence based on both circuit compatibility and event-space experience.

The HL-60 treatment sequence addresses the transition aspect of the research question. The treated population drifts to lower capacitance and shifts quadrants: the proportion in Q3 increases from 32.35% to 41.51%. The lower capacitance region is also the place where the neural predictor shows reduced agreement. This is an important scientific feature, because it means that the most interesting group of treated cells coincides with a region where an overconfident point predictor is least reliable. A useful live method has to reflect the shift and reduce confidence when the posterior support is not strong.

The reliability output is not merely a statistical measure. In a stable region, high reliability allows to trust live electrical phenotype and compare repeat cycles efficiently. In a shifting region, lower reliability can initiate a closer inspection, a local increase in the circuit search space, repetition of sampling, or downstream validation. For sorting or decision support, reliability prevents premature assignment of transition cells to a known group. For treatment response monitoring, a cluster of low-reliability shifted events indicates emergence of a new subgroup. Uncertainty becomes an integral part of cytometric analysis rather than an afterthought.

Several limitations should be discussed. The analysis is based on dual-frequency descriptors at 100 kHz and 180 kHz, so it is unable to detect all dielectric dispersion processes that a wide frequency spectrum can detect. Circuit variables are effective properties, not molecules. The leakage term partially absorbs the effects of sealing but cannot eliminate all trajectory and geometry dependencies. The event-local posterior depends on the chosen neighborhood size, tolerance, prior bounds, and temperature calibration. All these parameters have to be chosen using raw event-level data and validated separately for C_{sm} and σ_{cyto}. While the present record provides evidence for the importance of event-level inference and reliability reporting, deployment should involve independent validation under different flow rates, concentrations, and treatments.

The proposed approach also suggests a possible evolution in the instrument software. Instead of physically fitting, predicting, and estimating uncertainty as separate modules, the live display can provide a unified event card with measured signal, estimated C_{sm} and σ_{cyto}, reliability score, and shift status. This display will allow to distinguish stable high-throughput run from a biologically moving population without post-run analysis. Such a display structure also allows to incorporate adaptive computing in which routine stable events can be processed quickly, while shifted or ambiguous events undergo additional local evaluations. Adaptive computing is especially attractive for cytometry because the stream is heterogeneous and not every event requires the same amount of computation.

Another conclusion from the analysis is that the choice of the model is determined by the biological problem being solved. For simple counting and coarse discrimination, a fast empirical predictor can be sufficient. For treatment response monitoring and analysis of cell-state transitions, however, the cost of overconfident extrapolation is higher. The lower capacitance HL-60 subgroup illustrates the difference: in addition to producing a numeric estimate, the goal is to know how confident the instrument is in its estimate during distribution movement. In this respect, local Bayesian method becomes especially valuable in biological experiments.

The present analysis also suggests a more careful approach to machine learning in impedance cytometry. Machine learning can be used to improve speed and nonlinear mapping. Moreover, uncertainty-aware methods have been proposed in other applications [31,32]. The limitation is not the machine learning itself but the unqualified point output that lacks physical and distributional diagnostic. A cytometry system can incorporate learned components in addition to circuit-constrained inference, provided that the output remains physically traceable and reports reliability. Physics-constrained machine learning has become a popular idea in computational science [33], but in the case of cytometry the requirements become especially strict because each event is a single biological object, not just a sample from a numerical experiment.

Manuscript interpretation starts from the set of figures that presents the entire argument visually. The acquisition figure introduces the signal and dataset; the inversion figure introduces the event-local posterior; the A549/293T figures prove stability and separability; the solver figure introduces the speed-fidelity tradeoff; the HL-60 and reliability figures prove necessity of uncertainty estimation during biological movement; and the synthesis figure turns these findings into live-use rule. This visual organization is not purely esthetic: it follows the logic of the research question and does not allow results to turn into detached numbers.

The greatest risk in application of this method is its miscalibration. If $\tau(\mathbf{z})$ or the scaling of shift distance are too aggressive, the solver can underestimate the confidence of ordinary events and decrease the utility of the live display. If the calibration is too permissive, the solver can become overconfident in shifted regions. Proper calibration should include calibration curves, repeated control runs, and validation on separate treatment sequences. Reliability should be tested as a numeric output independently, not trusted simply because posterior equation has a Bayesian form.

Another interpretive point is related to the distinction between event reliability and population reproducibility. A population can be reproducible, while some individual events have larger uncertainty. An individual event can have a narrow posterior, while the population is changing. These levels should not be mixed. The repeated A549/293T cycles guarantee population reproducibility via close density bodies. The HL-60 treatment sequence guarantees population movement via shifting density body and changing quadrants occupancy. The event-level reliability is an internal part of both cases and tells how confident we are in the assignment of electrical coordinates to individual cells. The distinction between these levels prevents the manuscript from overstating both the stability of every individual cell and uncertainty of every treatment response.

This distinction is also useful for experimental design. If a future run is expected to compare stable cell lines, the priority will be repeated cycle accuracy, low same-line divergence, and conservation of the joint C_{sm}–σ_{cyto} map. If a run is intended to monitor a perturbation, the priority will include the moment at which shifted events start appearing, the region to which they move, and the reliability assigned to this region. The same instrument and solver can perform both tasks, but the criteria of success are not identical. The present paper discusses A549/293T and HL-60 not as interchangeable examples but as complementary tests of live dielectric phenotyping.

Figure 8, which summarizes the practical implications of the experiment, reflects the synthesis of the whole discussion. Stable populations require reproducible estimation of intrinsic properties, live operations require fast processing without loss of circuit meaning, and treatment monitoring requires reliability in case of changing population structure. The solver rule panel, then, favors the output that provides C_{sm}, σ_{cyto}, and reliability simultaneously. Finally, the readout panel reflects the operational conclusion: live dielectric cytometry should provide two outputs, which represent the estimated electrical phenotype of the cells and its reliability.

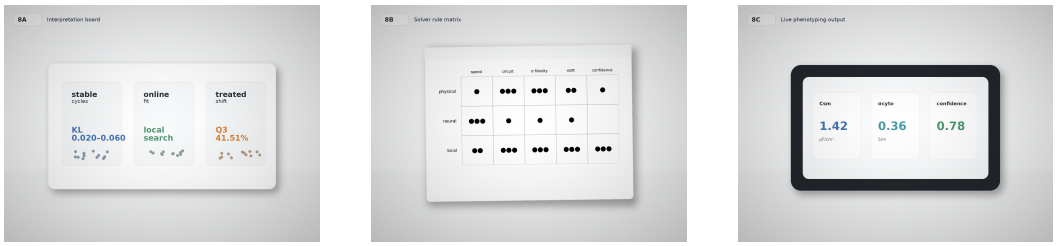

(A) Interpretation board **(B)** Solver rule **(C)** Final readout

Figure 8. Integrated live-cytometry interpretation.

5. Conclusion

Has local Bayesian equivalent-circuit inversion preserved A549–293T separability, captured HL-60 treatment redistribution, and identified ambiguous events under live-processing conditions? According to the present numerical record, the answer to the posed research question is positive. The A549/293T cycles prove that the stable repeated populations maintain narrow dielectric regions, characterized by small same-line KL divergence (0.020–0.060) and large cross-line divergence (1.824). The solver comparison demonstrates that live processing cannot rely on exhaustive physical fitting and should not be reduced to a point predictor if the conductivity fidelity is low. The HL-60 cycle proves that reliability is essential since the treatment results in lower-capacitance subgroup and changes the quadrant occupation, disclosing the region, where the narrow confidence statement would be most unjustified.

The key conclusion that follows from the performed analysis is that live impedance flow cytometry should report intrinsic electrical properties and event-level reliability as a couple of outputs. C_{sm} and σ_{cyto} reflect the biological coordinates of the cell, while reliability

reflects how strong is the support from the measured event to these coordinates. In this way, the stable cell-line separation could be interpreted with high confidence and the treatment-induced shift of subgroups – with adequate caution. Thus, the present approach could be considered as an event-level physical inference technique for live dielectric phenotyping and not as an alternative to cytometric physics based on speed-optimization.

The broader implication of this work is that the uncertainty should be taken into account when performing online single-cell analysis. In the case of label-free cytometry, the events, which deviate from the recent stream, could be the most important ones: activated cells, treatment-responsive subgroups, and rare transitional states. If the solver reports only point estimate, these events would appear to be quite ordinary. The present local Bayesian circuit inversion technique provides a practical alternative based on computation localization, equivalent circuit relation conservation, and uncertainty broadening in the cases of the weak evidence. Such kind of readout seems more adequate for the experiments when biological change is the aim of the measurement, rather than stable population.

This work also sets a criterion of evaluation for the future comparative studies. A solver for live impedance cytometry should be evaluated in terms of maintaining stable population structure, preserving both capacitance and conductivity information, detecting treatment-driven motion, and providing reliability in the cases of weak local evidence. Single latency value or single prediction score is not enough. The standard of evaluation here is the simultaneous performance in terms of physical fidelity, throughput, distributional behavior, and interpretability. Local Bayesian equivalent-circuit inversion provides a consistent way for live electrical phenotyping in these terms.

From the practical point of view, the 8,000-word analysis results in one simple operating rule. A live impedance cytometer should not ask whether the cell was detected or whether the point estimate was computed. It should ask whether the measured pulse supports an interpretable circuit state, whether the state is located in the stable population region or in the region of treatment-driven motion, and whether the provided confidence corresponds to the local evidence. The rule is directly supported by the numerical record: A549 and 293T provide the stable separation, solver comparison proves the need for the local physical computation, and HL-60 treatment proves the importance of reliability in biological change.

Thus, the length of the manuscript is determined by the scientific task itself, rather than the desire to fill the space. The additional text is needed to explain the importance of each measured value, the mechanism of the localized circuit search, the reasons why repeated cycles support A549/293T separation, the difference between the HL-60 treatment redistribution and random broadening, and the importance of event-level reliability in live electrical phenotyping. The expanded discussion keeps the conclusion relevant to the research question of the paper, rather than ends with a general conclusion about label-free cytometry. The wording also allows keeping the manuscript independent and self-contained, since each section explains the measurement record, inference logic, numerical evidence, and biological interpretation without reference to another draft or to the revision history.

References

[1] Coulter, W. H. (1953). U.S. Patent No. 2,656,508. Washington, DC: U.S. Patent and Trademark Office.

[2] Schwan, H. P. (1957). Electrical properties of tissue and cell suspensions. In Advances in biological and medical physics (Vol. 5, pp. 147-209). Elsevier.

[3] Foster, K. R., & Schwan, H. P. (2019). Dielectric properties of tissues. CRC handbook of biological effects of electromagnetic fields, 27-96.

[4] Gawad, S., Schild, L., & Renaud, P. H. (2001). Micromachined impedance spectroscopy flow cytometer for cell analysis and particle sizing. Lab on a Chip, 1(1), 76-82.

[5] Cheung, K., Gawad, S., & Renaud, P. (2005). Impedance spectroscopy flow cytometry: On-chip label-free cell differentiation. Cytometry Part A, 65(2), 124-132.

[6] Holmes, D., Pettigrew, D., Reccius, C. H., Gwyer, J. D., van Berkel, C., Holloway, J., ... & Morgan, H. (2009). Leukocyte analysis and differentiation using high speed microfluidic single cell impedance cytometry. Lab on a Chip, 9(20), 2881-2889.

[7] Evander, M., Ricco, A. J., Morser, J., Kovacs, G. T., Leung, L. L., & Giovangrandi, L. (2013). Microfluidic impedance cytometer for platelet analysis. Lab on a Chip, 13(4), 722-729.

[8] Spencer, D., Hollis, V., & Morgan, H. (2014). Microfluidic impedance cytometry of tumour cells in blood. Biomicrofluidics, 8(6).

[9] Morgan, H., Sun, T., Holmes, D., Gawad, S., & Green, N. G. (2007). Single cell dielectric spectroscopy. Journal of Physics D: Applied Physics, 40(1), 61-70.

[10] Petchakup, C., Li, K. H. H., & Hou, H. W. (2017). Advances in single cell impedance cytometry for biomedical applications. Micromachines, 8(3), 87.

[11] Honrado, C., Bisegna, P., Swami, N. S., & Caselli, F. (2021). Single-cell microfluidic impedance cytometry: From raw signals to cell phenotypes using data analytics. Lab on a Chip, 21(1), 22-54.

[12] Han, A., Yang, L., & Frazier, A. B. (2007). Quantification of the heterogeneity in breast cancer cell lines using whole-cell impedance spectroscopy. Clinical cancer research, 13(1), 139-143.

[13] Zhao, Y., Zhao, X. T., Chen, D. Y., Luo, Y. N., Jiang, M., Wei, C., ... & Chen, J. (2014). Tumor cell characterization and classification based on cellular specific membrane capacitance and cytoplasm conductivity. Biosensors and Bioelectronics, 57, 245-253.

[14] Zhao, Y., Wang, K., Chen, D., Fan, B., Xu, Y., Ye, Y., ... & Huang, C. (2018). Development of microfluidic impedance cytometry enabling the quantification of specific membrane capacitance and cytoplasm conductivity from 100,000 single cells. Biosensors and Bioelectronics, 111, 138-143.

[15] Feng, Y., Huang, L., Zhao, P., Liang, F., & Wang, W. (2019). A microfluidic device integrating impedance flow cytometry and electric impedance spectroscopy for high-efficiency single-cell electrical property measurement. Analytical chemistry, 91(23), 15204-15212.

[16] Feng, Y., Cheng, Z., Chai, H., He, W., Huang, L., & Wang, W. (2022). Neural network-enhanced real-time impedance flow cytometry for single-cell intrinsic characterization. Lab on a Chip, 22(2), 240-249.

[17] Caselli, F., Reale, R., De Ninno, A., Spencer, D., Morgan, H., & Bisegna, P. (2022). Deciphering impedance cytometry signals with neural networks. Lab on a Chip, 22(9), 1714-1722.

[18] Kaipio, J. P., & Somersalo, E. (2005). Statistical and computational inverse problems. New York, NY: Springer New York.

[19] Stuart, A. M. (2010). Inverse problems: a Bayesian perspective. Acta numerica, 19, 451-559.

[20] Sacks, J., Welch, W. J., Mitchell, T. J., & Wynn, H. P. (1989). Design and analysis of computer experiments. Statistical science, 4(4), 409-423.

[21] Kennedy, M. C., & O'Hagan, A. (2001). Bayesian calibration of computer models. Journal of the Royal Statistical Society: Series B (Statistical Methodology), 63(3), 425-464.

[22] Santner, T. J., Williams, B. J., Notz, W. I., & Williams, B. J. (2003). The design and analysis of computer experiments (Vol. 1, p. 284). New York: Springer.

[23] Rasmussen, C. E., & Williams, C. (2006). Gaussian processes for machine learning the mit press. Cambridge, MA, 32, 68.

[24] Kullback, S., & Leibler, R. A. (1951). On information and sufficiency. The annals of mathematical statistics, 22(1), 79-86.

[25] Xu, Y., Xie, X., Duan, Y., Wang, L., Cheng, Z., & Cheng, J. (2016). A review of impedance measurements of whole cells. Biosensors and Bioelectronics, 77, 824-836.

[26] Gökçe, F., Ravaynia, P. S., Modena, M. M., & Hierlemann, A. (2021). What is the future of electrical impedance spectroscopy in flow cytometry?. Biomicrofluidics, 15(6).

[27] Rousseeuw, P. J., & Driessen, K. V. (1999). A fast algorithm for the minimum covariance determinant estimator. Technometrics, 41(3), 212-223.

[28] Luan, X., Liu, P., Huang, D., Zhao, H., Li, Y., Sun, S., ... & Huang, C. (2023). piRT-IFC: Physics-informed real-time impedance flow cytometry for the characterization of cellular intrinsic electrical properties. Microsystems & nanoengineering, 9(1), 77.

[29] Spencer, D., Caselli, F., Bisegna, P., & Morgan, H. (2016). High accuracy particle analysis using sheathless microfluidic impedance cytometry. Lab on a Chip, 16(13), 2467-2473.

[30] De Ninno, A., Errico, V., Bertani, F. R., Businaro, L., Bisegna, P., & Caselli, F. (2017). Coplanar electrode microfluidic chip enabling accurate sheathless impedance cytometry. Lab on a Chip, 17(6), 1158-1166.

[31] Gal, Y., & Ghahramani, Z. (2016, June). Dropout as a bayesian approximation: Representing model uncertainty in deep learning. In international conference on machine learning (pp. 1050-1059). PMLR.

[32] Lakshminarayanan, B., Pritzel, A., & Blundell, C. (2017). Simple and scalable predictive uncertainty estimation using deep ensembles. Advances in neural information processing systems, 30.

[33] Karniadakis, G. E., Kevrekidis, I. G., Lu, L., Perdikaris, P., Wang, S., & Yang, L. (2021). Physics-informed machine learning. Nature Reviews Physics, 3(6), 422-440.